11th International Symposium on Turbulence and Shear Flow Phenomena (TSFP11)
Southampton, UK, July 30 to August 2, 2019

# EXPERIMENTAL STUDY OF TURBULENT FARADAY INSTABILITY IN MISCIBLE FLUIDS

**Louis Gostiaux**
Univ Lyon, École Centrale de Lyon, INSA Lyon,
Université Claude Bernard Lyon I, CNRS,
LMFA, UMR 5509,
36 Avenue Guy de Collongue, F-69134, ECULLY, France
louis.gostiaux@ec-lyon.fr

**Benoît-Joseph Gréa**
DIF, DAM, CEA
Arpajon, France
benoit-joseph.grea@cea.fr

**Antoine Briard**
CMLA, ENS Cachan, CNRS
Université Paris-Saclay
94235 Cachan, France
antoine.briard@hotmail.fr

## INTRODUCTION

We characterized experimentally the turbulent mixing at a fluid interface subject to vertical accelerations. It is known since Faraday (1831) that when a container partly filled with liquid vibrates, its free surface becomes unstable and regularly corrugates. This phenomenon has been interpreted in the case of a vertically oscillating container as a parametric instability (Benjamin & Ursell, 1954), and extensively studied since then with a good agreement between theory and experiment (Ciliberto & Gollub, 1985; Douady & Fauve, 1988; Douady, 1990). This instability does not only concern free surfaces, but also interfaces between two immiscible fluids, for which the dispersion relation and the resonance conditions are modified by the inertia of the upper fluid (Kumar & Tuckerman, 1994).

All the above mentioned studies are dealing with immiscible fluids, where surface tension plays a role in the development of the instability. Since then, only one experiment has observed the instability at the interface between two miscible fluids accelerated vertically (Zoueshtiagh *et al.*, 2009). Recently, Gréa & Ebo Adou (2018) have provided, using the stability diagram of Mathieu equations, a prediction for the saturation of the instability. As the mean gradient decreases with time due to turbulent mixing, the thickness of the interface saturates at

$$L_{sat} = 2\mathscr{A}_t G_0 (2F+4)/\omega^2, \qquad (1)$$

where $G_0$ is the gravitational acceleration, $F$ the forcing intensity (ratio of the maximal vertical acceleration to the gravitationnal acceleration), $\omega$ the forcing pulsation, and $\mathscr{A}_t = \frac{(\rho_2-\rho_1)}{(\rho_1+\rho_2)}$ the Atwood number. This prediction was verifieded numerically (Gréa & Ebo Adou, 2018), as well as the transition from harmonic to subharmonic regime (Briard *et al.*, 2019), but the experimental validations required a set-up of sufficiently large dimensions. This is the purpose

Figure 1. Experimental setup. Top : general view of the platform on the hexapod. The experimental tank is empty, and enlighted from the back by a LED panel. The arm holding the camera is visible. Bottom : experimental tank filled with two layer miscible fluid, before the experiment. Note the initial sharpness of the interface. Blue dye is added in the fresh layer for measurement.

of the present study, for which the scale of the experiment has been increased by a factor of 100 in comparison with Zoueshtiagh *et al.* (2009). In this case, a fully tyrbulent regime is observed and characterized in the experiments.

## EXPERIMENTAL SETUP

The experiment consisted of a parallepipedic plexiglas tank of inner dimensions $94 \times 67 \times 11cm^3$, initially designed for free-surface flow studies at the Gaztransport and Technigaz (GTT) platform motion analysis and testing laboratory, and visible on Figure 1. Fluid was injected in the container through a bottom diffuser, first with pure water colored with food dye (Patented blue), then slowly adding densier salty water (using commercial softening agent). The density difference between the two fluids ranged between 10 and 100 $kg/m^3$, where pure water had a constant density of $\rho_1 = 998kg/m^3$. The whole tank was tightly attached to the platform of three different ©Symetrie hexapods of the GTT laboratory, providing vertical accelerations up to $F = 0,7$. The motion imposed consisted of a series of $n$ vertical oscillations $z(t) = a\cos(\omega(t-t_0))$, starting at $t = t_0 = 20s$ and ending at $t = t_0 + n * \frac{2\pi}{\omega}$. Before the experiment, the platform was slowly sent to $z = a$, and at the end of the oscillations cycle, the platform stood at $z = a$ for 20s, and was then slowly sent back to $z = 0$. Note that the choice of a cos function, along with oscillations starting and stopping at $z = a$, ensured that no additional acceleration was introduced at the beginning and at the end of the forcing. For this reason, no ascending or descending ramp was introduced in the forcing.

A temperature-conductivity ©MSTCI PME probe was used to measure the density profile in the tank before and after each experiment. The probe was fixed above the tank, and the vertical motion of the hexapod was used to let the probe pass through the interface. A 12-bits ©IDS monochromatic video camera, filtered in the red by a general purpose gelatine filter, captured at 45fps the image of a LED back-lightened white screen seen throught the tank. The camera was attached to the oscillating platform by means of a $1.5m$ long ©Elcom arm, mechanically inforced to minimize vibrations. A picture of the experimental setup is visible on Figure 1, and a set of three images captured by the camera is shown on Figure 3. The image intensity was converted, using Beer-Lambert law and a point by point intensity calibration accounting for background inhomogeneities, into an instantaneous, cross-tank integrated, field of density. The obtained density field was compared, before and after each experiment, to the measurement of the density probe in order to validate the calibration. The density field $\rho(x,z,t)$ was normalized so that for the initial condition $\rho^* = 1$ in the dense region and $\rho^* = 0$ in the light region.

## RESULTS

A first session of 8 experiments was performed in August 2018 at the GTT research center. A second session of 47 runs was conducted in october 2018, the results of which will be presented in the present proceeding. The experimental parameters covered by the experiments are listed on Table 1, and represented in the $F - \omega$ plane on Figure 2. In this diagram, the three curves indicate the limitations of the three different hexapods used during the campaign. The different parts of che curve correspond to limitations in amplitude, speed and acceleration, as $\omega$ increases.

Table 1. Parameters of the 47 experiments. Column camera matches the experiments where data from the camera are available with a x. Column Probe matches the esperiments where a density profile was available before (b) and after (a) the experiment.

| Run | Camera | Probe | $\mathscr{A}_t$ | $\omega$ | F |
|---|---|---|---|---|---|
| run01 | x | | 0.015 | 3.46 | 0.6 |
| run02 | x | ba | 0.015 | 3.46 | 0.6 |
| run03 | x | | 0.015 | 2.95 | 0.4 |
| run04 | | ba | 0.015 | 2.55 | 0.3 |
| run05 | x | | 0.015 | 2.55 | 0.3 |
| run06 | x | | 0.030 | 4.52 | 0.3 |
| run07 | x | ba | 0.030 | 3.02 | 0.2 |
| run08 | | | 0.030 | 3.02 | 0.2 |
| run09 | x | | 0.015 | 2.13 | 0.3 |
| run10 | x | | 0.015 | 3.92 | 0.6 |
| run11 | x | | 0.015 | 2.13 | 0.3 |
| run12 | x | | 0.015 | 4.29 | 0.7 |
| run13 | x | | 0.015 | 1.73 | 0.2 |
| run14 | x | | 0.030 | 4.29 | 0.7 |
| run15 | x | | 0.030 | 2.46 | 0.4 |
| run16 | x | | 0.030 | 4.29 | 0.7 |
| run17 | x | | 0.030 | 2.46 | 0.4 |
| run18 | | | 0.030 | 4.29 | 0.7 |
| run19 | x | b | 0.030 | 4.29 | 0.7 |
| run20 | x | | 0.045 | 2.46 | 0.4 |
| run21 | x | | 0.045 | 4.29 | 0.7 |
| run22 | x | | 0.045 | 3.92 | 0.6 |
| run23 | x | | 0.045 | 4.29 | 0.7 |
| run24 | x | a | 0.015 | 4.29 | 0.7 |
| run25 | x | ba | 0.015 | 4.29 | 0.7 |
| run26 | x | ba | 0.030 | 4.29 | 0.7 |
| run27 | x | a | 0.030 | 4.29 | 0.7 |
| run28 | x | | 0.030 | 4.00 | 0.7 |
| run29 | | ba | 0.030 | 3.14 | 0.5 |
| run30 | x | ba | 0.015 | 3.14 | 0.5 |
| run31 | | ba | 0.015 | 3.92 | 0.5 |
| run32 | x | ba | 0.015 | 3.92 | 0.5 |
| run33 | x | ba | 0.015 | 2.46 | 0.4 |
| run34 | x | ba | 0.015 | 3.92 | 0.4 |
| run35 | x | | 0.030 | 4.29 | 0.7 |
| run36 | x | | 0.030 | 2.46 | 0.4 |
| run37 | x | ba | 0.030 | 4.52 | 0.5 |
| run38 | x | ba | 0.030 | 3.14 | 0.5 |
| run39 | x | ba | 0.030 | 4.29 | 0.7 |
| run40 | x | ba | 0.045 | 4.29 | 0.7 |
| run41 | x | ba | 0.030 | 3.46 | 0.4 |
| run42 | x | ba | 0.045 | 3.07 | 0.5 |
| run43 | x | ba | 0.015 | 3.46 | 0.4 |
| run44 | x | ba | 0.015 | 2.95 | 0.3 |
| run45 | x | ba | 0.015 | 3.46 | 0.3 |
| run46 | x | ba | 0.015 | 3.92 | 0.3 |
| run47 | | ba | 0.045 | 3.92 | 0.6 |

An example of three raw images taken before, during and after forcing for Run 21 is shown on Figure 3. When comparing the images before and after the experiment, the irreversible thickening of the interface is clearly visible, as a result of turbulent mixing at the instable interface. On the image taken during the forcing, the interface, although turbulent, presents a dominant wavelength which is governed by the longest dimension of the tank and the stratification. As the stratification evolves with time, successive resonances are observed and will be studied more in details by means of a linear stability analysis inspired by Kumar & Tuckerman (1994).

The interface thickness $L(t)$ was computed from the images using the formula

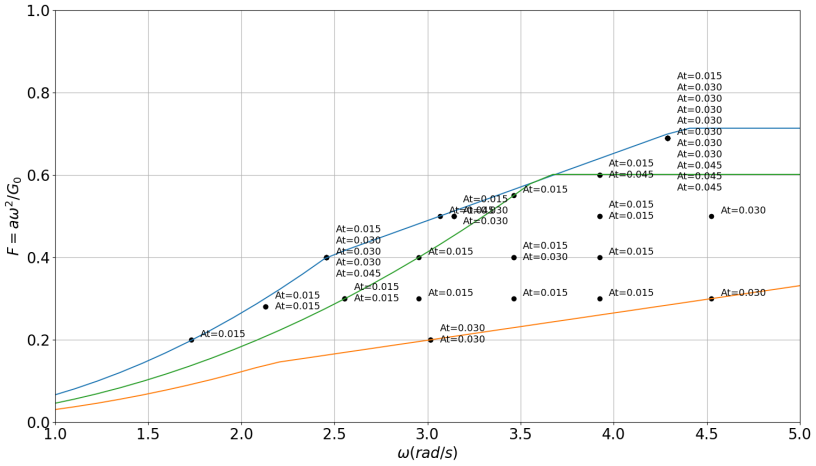


Figure 2. Location of the experimental runs in the $F-\omega$ plane. At each location, the different experiments performed are listed according to their Atwood number.

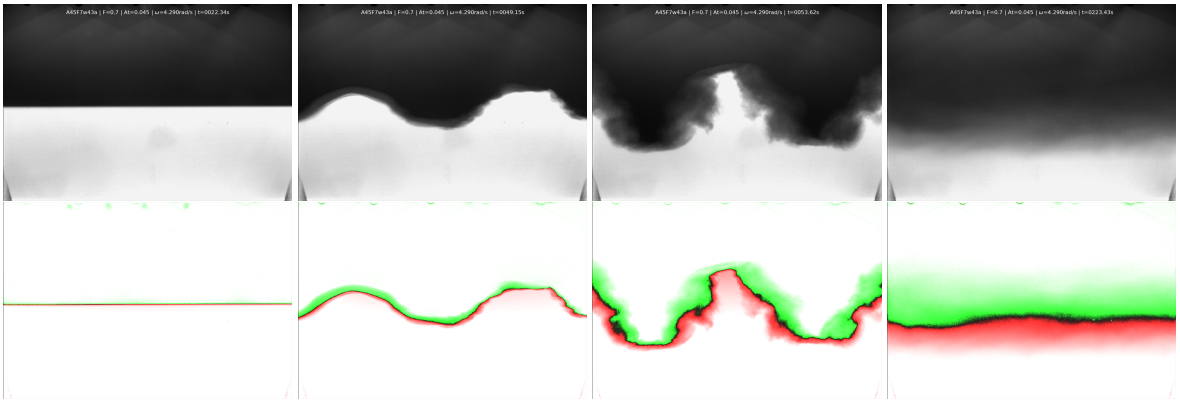

Figure 3. Raw images captured during Run 21 at the beginning of the experiment, at t=49s, at t=54s, and at the end of the experiment. The inhomogeneities in enlightment visible in the upper and lower parts are removed when estimating the attenuation used in Beer Lambert law, as can be seen in the calibrated images on the second row.

$$L(t) = 6\int \bar{\rho}^*(1-\bar{\rho}^*)dz \qquad (2)$$

where $\bar{\rho}^*(z)$ is the horizontally averaged normalized density field (Gréa & Ebo Adou, 2018).

The time evolution of $L(t)$ is shown on Figure 4 (top) for Run 21, where the oscillations started at t=20s. The oscillations of the interface are subharmonic, leading to an harmonic oscillation of the interface thickness $L(t)$. The theoretical value for the saturation length $L_{sat}$ is remarkably recovered. The prediction is in fact valid for all the 47 different experiments, with different Atwood numbers, frequencies and forcing amplitudes, as can be seen on Figure 4 (bottom).

A set of dedicated $1024^3$ Direct Numerical Simulation of the experiment have been performed, taking into account of the finite size of the tank by introducing a penalization. If not only the value of the saturated state, but also the growth rate of the instability is quantitatively reproduced, some differences remain at the early stage of the instability, that are attributed to Schmidt number effects (set to 1 in the simulations, instead of 700 for salt in the experiments). The existence of a harmonic to subharmonic transition (Briard *et al.*, 2019) at the onset of the instability has also been studied experimentally and numerically.

## ACKNOWLEDGEMENT

This research benefited from the installations of Gaztransport and Technigaz Platform motion Analysis and Testing Laboratory, with the assistance of Y. Atik, S. Moreau and A. Landure.

## REFERENCES

Benjamin, T. B. & Ursell, F. 1954 The stability of the plane free surface of a liquid in vertical periodic motion. *Proceedings of the Royal Society of London A* **225** (1163), 505–515.

Briard, Antoine, Gréa, Benoît-Joseph & Gostiaux, Louis 2019 Harmonic to subharmonic transition of the faraday instability in miscible fluids. *Physical Review Fluids* **4**, 044502.

Ciliberto, S. & Gollub, J. P. 1985 Chaotic mode competition in parametrically forced surface waves. *Journal of Fluid Mechanics* **158**, 381–398.

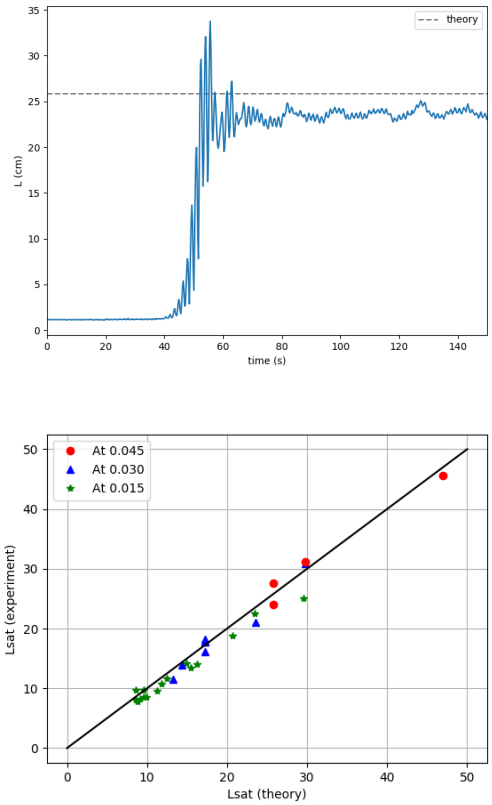


Figure 4. Top : evolution of the interface thickness L(t) for Run 21. The dashed line corresponds to the theoretical prediction of (Gréa & Ebo Adou, 2018). Bottom : comparison between therotecial prediction of Eq. 1 for the saturation length, with measurements.

Douady, S. 1990 Experimental study of the faraday instability. *Journal of Fluid Mechanics* **221**, 383–409.

Douady, S. & Fauve, S. 1988 Pattern selection in faraday instability. *EPL (Europhysics Letters)* **6** (3), 221.

Faraday, Michael 1831 On a peculiar class of acoustical figures; and on certain forms assumed by groups of particles upon vibrating elastic surfaces. *Philosophical Transactions of the Royal Society of London* **121** (XVII), 299–340.

Gréa, B.-J. & Ebo Adou, A. 2018 What is the final size of turbulent mixing zones driven by the faraday instability? *Journal of Fluid Mechanics* **837**, 293–319.

Kumar, Krishna & Tuckerman, Laurette S. 1994 Parametric instability of the interface between two fluids. *Journal of Fluid Mechanics* **279**, 49–68.

Zoueshtiagh, F., Amiroudine, S. & Narayanan, R. 2009 Experimental and numerical study of miscible faraday instability. *Journal of Fluid Mechanics* **628**, 43–55.